

# 1 Glass/steel/clay interactions in a simulated radioactive waste geological disposal system

2 I. Tolnai, J. Osan, O. Czompoly, A. Sulyok, M. Fabian\*

3  
4 *Centre for Energy Research, Konkoly Thege St. 29-33., Budapest, 1121, Hungary*

5  
6 \*Corresponding Author: [fabian.margit@ek-cer.hu](mailto:fabian.margit@ek-cer.hu), ORCID: 0000-0002-6528-4695

## 7 8 **Abstract**

9 Deep geological storage is the accepted solution for the final disposal of high level radioactive  
10 waste therefore, it is necessary to study the host rock of the planned Hungarian waste  
11 repository and the materials involved in the engineered barriers. The main goal was to  
12 understand the characteristics and stability of the glass/steel/claystone system, from the  
13 structural properties of the vitrified waste (borosilicate glasses) to the clay response in the  
14 repository. Repository conditions were applied during the experiments to understand the  
15 chemical evolution of the system. A triplicate setup was kept at 80°C for 3, 7 and 12 months  
16 and post-mortem characterization was performed. No alteration products were observed with  
17 scanning electron microscopy energy dispersive X-ray spectroscopy measurements on the  
18 surface of the glass and Fe or in the clay after the end of the experimental period. Based on  
19 the elemental analysis of the leachates, the released amount of B, K, Si and K increases over  
20 time, while that of Ca and Mg decreases. The concentrations of Cl<sup>-</sup> and SO<sub>4</sub><sup>2-</sup> did not change  
21 significantly. Ca- and Mg-silicate precipitation was observed by X-ray photoelectron  
22 spectroscopy at the surface range of the borosilicate glasses due to the effect of the synthetic  
23 porewater treatment.

## 24 **Introduction**

25 Nuclear energy is one of the safest and cleanest forms of electricity generation. The Paks  
26 Nuclear Power Plant covers almost half (~46%) of the electricity production in Hungary,  
27 similarly high values can be observed in other countries with nuclear power plants <sup>1</sup>. To  
28 achieve sustainability, a great significance must be placed on the treatment and disposal of  
29 high-level radioactive waste (HLW) generated during normal operation <sup>2</sup>. HLW primarily  
30 include the spent fuel (SF), as well as the waste generated by the technology during  
31 reprocessing of SF <sup>3</sup>. SF rods are first sent to storage pools for short-term cooling, then  
32 transferred to wet or dry storage facilities where these await either reprocessing or deep

33 geological disposal <sup>4</sup>. The multi-barrier system is responsible for long-term safe storage by  
34 isolating the radioactive waste from the biosphere in deep geological repositories. Achieving  
35 this goal requires both natural geological barriers and engineered barrier system (EBS) with  
36 complementary safety functions, creating a robust system to enhance confidence in the  
37 protection that will be provided. The EBS itself comprise a variety of sub-systems such as the  
38 waste form (radioactive material immobilized in a host material), a corrosion resistant and  
39 mechanically stable container, a buffer/sealing system, and plugs. The EBS must be designed  
40 so that it will work with the natural barriers to meet the regulatory limits <sup>5, 6</sup>. A common  
41 practice to handle and treat HLW materials is to embed them in a suitable host matrix through  
42 the process of vitrification. Glass matrices are often used for this purpose being due to their  
43 excellent chemical and mechanical parameters, their thermodynamic stability and radiation  
44 resistance are also adequate <sup>789</sup>. The vitrified HLW material is placed in a metal canister,  
45 which in most cases is made of carbon steel or stainless steel. The choice of its grade largely  
46 depends on the type of the material to be stored as well as the undesirable effects caused by  
47 the geological environment considering the goal is to ensure the containment of the  
48 radioactive material for more than 100,000 years. The buffer/sealing materials are responsible  
49 for the stability of the deep geological repository through providing desired mechanical,  
50 chemical, hydro-mechanical and thermal conditions and are characterized by low permeability  
51 and diffusivity and ensure long term retardation <sup>610</sup>.

52 The aim of our work was to study the chemical evolution of a glass/steel/clay system held  
53 under conditions like those that could be predicted in a deep geological repository. Long-term  
54 exposure to repository conditions could result in significant alterations on EBS materials  
55 during the service life. The host media can be source of oxygen, reactive ions and other  
56 species that can cause significant alterations to the system during its operation. The effects of  
57 radiation, temperature and mechanical stress must also be considered when various form of  
58 degradation is calculated <sup>101112</sup>.

59 Scale model systems were assembled such a way that close to real conditions were provided.  
60 Our model EBS comprises borosilicate glass; modelling the waste matrix, iron; modelling the  
61 steel canister and claystone; modelling the low permeability buffer. The main goal was to  
62 understand characteristics, applicability, and stability of the whole system, from the structural  
63 properties of the vitrified waste to the clay response in the repository. Here, we demonstrate  
64 the characterization of a borosilicate glass/iron/clay model system using scanning electron  
65 microscopy energy dispersive X-ray spectroscopy and X-ray photoelectron spectroscopy. The

66 identifications and compositions of these materials provide information on the iron and glass  
67 alteration in function of applied conditions. With the Inductively Coupled Plasma Optical  
68 Emission Spectroscopy and Ion Chromatography we predict the chemical durability of the  
69 system, thanks to the obtained leachates at the all stage of the experiments.

## 70 **Design of the experiment**

### 71 *Materials*

72 The composition of the 5-component sodium borosilicate glassy specimen was 55mol%SiO<sub>2</sub>-  
73 10mol%B<sub>2</sub>O<sub>3</sub>-25mol%Na<sub>2</sub>O-5mol%BaO-5mol%ZrO<sub>2</sub>, with a density of 2.67 g/cm<sup>3</sup>. Synthesis  
74 and basic structural properties of the applied borosilicate glass was presented in an earlier  
75 study<sup>13</sup>.

76 Fe flakes (99%, from Acros Organics, CAS Nr. 7439-89-6) of 50-68 μm particle diameter  
77 fraction was used for the experiment. The size range was based on the consideration that the  
78 size of all three components should be commensurable during the experiments.

79 Boda Claystone Formation (BCF) is considered as the potential host rock system of the HLW  
80 repository in Hungary. The Boda Block of BCF forms an anticline structure. In this block the  
81 maximum thickness of the BCF varies between 700-1000 meters in the central region. During  
82 the sedimentation catagenetic stage was finally reached under high temperature (200-250 °C)  
83 and pressure (120-150 MPa). Six main rock types of BCF can be defined based on  
84 mineralogical, geochemical, and textural considerations: albitic claystone, albitolite, „true”  
85 siltstone, dolomite interbeddings, sandstone and conglomerata. The BCF has the following  
86 parameters: porosity (%): min: 0.6-max: 1.4; hydraulic conductivity (m/s): 10<sup>-11</sup>-10<sup>-13</sup>; solid  
87 density (kg/m<sup>3</sup>): 2300-2700<sup>1415</sup>. Since albitic claystone is the most dominant rock type of the  
88 formation<sup>16</sup>, a representative section of the BAF-2 drilling core was selected for the present  
89 study. **Table 1** contains its mineralogical composition.

90 During the experiments the crushed BCF claystone was steeped with synthetic porewater  
91 resulting in a saturation of 100%. The initial BCF porewater considered in the experiment was  
92 a modeled synthetic porewater. The calculations of the Boda porewater chemistry were  
93 performed with the geochemical speciation code MINSORB and the Nagra/PSI 01/01  
94 thermodynamic database<sup>1718</sup>. The chemical composition of the Boda porewater was calculated  
95 at fixed  $p_{CO_2}$  (= 10<sup>-3.5</sup> bar)/pH (= 8.0) i.e., in equilibrium with atmospheric  $p_{CO_2}$ , and under the  
96 constraint of calcite, dolomite and quartz saturation. Na<sup>+</sup> or Cl<sup>-</sup> concentration was adjusted to  
97 maintain charge neutrality, while Ca, Mg, Si and C(IV) concentrations were defined over the

98 above boundary conditions <sup>19</sup>. The synthetic Boda porewater (SBPW) composition is given in  
99 **Table 2**.

#### 100 *Experimental setup*

101 To get information on the effect of the long-term exposure a scaled-down model system was  
102 assembled close to disposal conditions to understand the chemical evolution of the contacting  
103 materials, and stability of the system from the structural and dissolution properties of the  
104 modelled vitrified waste to the clay response in the repository. Our experiment was carried  
105 out with three pieces of such glass/steel/clay model setup as shown in Fig. 1.

106 To provide the necessary physical conditions, the prepared setup was embedded into an  
107 external and an internal Teflon container. During the experiments all the three setups were  
108 fully saturated by SBPW. The internal vessel contained the mixture of 1.4 g of powdered  
109 glass (borosilicate powder, 50-86  $\mu\text{m}$  particle size, 0.083  $\text{m}^2$  surface area) <sup>13</sup>, 0.7 g of steel (Fe  
110 powder, 50-86  $\mu\text{m}$  particle size, 0.008  $\text{m}^2$  surface area) and 27.9 g of claystone (crushed Boda  
111 albitic claystone, <100  $\mu\text{m}$  fraction) <sup>19</sup>. The conditioning of Boda claystone with the applied  
112 SBPW was carried out at room temperature. The external vessel contained the enclosed  
113 internal vessel that was surrounded by 75.36 ml of SBPW (see Fig. 1). During the static  
114 experiments, the shape of the glass grains was assumed to be cubic so that the calculated  
115 surface area to volume ratio ( $SA/V$ ) was 1108  $\text{m}^{-1}$ . To ensure the continuous saturation,  
116 randomly holes with 0.7 mm diameter were drilled on the wall of the internal vessels. All the  
117 containers were filled with the same glass/steel/clay mixture and kept in an incubator at 80  
118  $^{\circ}\text{C}$ . After 3, 7 and 12 months a container was opened for post-mortem characterization and  
119 named as GFeC-3M, GFeC-7M and GFeC-12M, respectively. A portion of the initial  
120 glass/steel/clay mixture was preserved and kept dry for reference, and the used SBPW was  
121 also preserved for similar purposes.

#### 122 *Sample preparation for post-mortem characterization*

123 For morphological measurements, 5 g of samples were taken from the inner Teflon  
124 containers, and 13 mm diameter pellets were prepared using a SPECAC KBR 25.011  
125 hydraulic press. No binder compound was needed because the applied high pressure  
126 procedure resulted in a solid pellet

#### 127 *Glass sample preparation for X-ray photoelectron spectroscopy measurements*

128 X-ray photoelectron spectroscopy (XPS) measurements were performed on separate glassy  
129 samples with composition of 55mol%SiO<sub>2</sub>-10mol%B<sub>2</sub>O<sub>3</sub>-25mol%Na<sub>2</sub>O-5mol%BaO-5mol  
130 %ZrO<sub>2</sub> in order to study the effect of the synthetic Boda porewater treatment at the surface  
131 range combined with the elevated temperature. For this purpose, another triplicate system was  
132 used which consisted of one Teflon container with the glass sample inside, which was  
133 immersed in SBPW, the calculated SA/V was 2000 m<sup>-1</sup>. The samples were heat treated the  
134 same way at 80 °C for 1, 2 and 3 months. The samples are labeled G-1M, G-2M and G-3M,  
135 with the number referring to the duration of the treatment and a reference sample without  
136 treatment was used, labeled as G-Ref.

## 137 **Results and discussion**

### 138 *Electron microscopy of the post-mortem samples*

139 Scanning electron microscopy energy dispersive X-ray spectroscopy (SEM/EDX)  
140 investigations were focused on the possible crystallization and homogeneity of the glass and  
141 the nature of alteration products formed on its surface as well as the composition of the Fe and  
142 clay.

143 Detailed SEM images for the GFeC-3M, GFeC-7M and GFeC-12M are shown in Fig. 2, Fig.  
144 3 and Fig. 4, respectively. Based on the recorded images the structure of iron and glass did not  
145 change significantly during the experiment. Both the edges and the bulk phase remained  
146 uniform and homogeneous; no alteration layers were formed. Table 3, Table 4 and Table 5  
147 contains the major elemental composition for the selected positions. The elemental  
148 composition of the glass particles was rather similar in the case of the GFeC-3M and GFeC-  
149 12M samples meaning that the average composition within the information depth (~1 μm) did  
150 not change as a result of the experimental treatment. However, a slight alteration in the  
151 composition can be observed in the GFeC-7M sample. A difference can be measured in O, Si,  
152 Zr and Ba content as similar changes were reported in Ref. <sup>20</sup>. Spec2 in Table 4 shows a Si  
153 content of 23.0%, while Spec3 in Table 4 shows 31.6%, this difference can be explained with  
154 partial hydration of the glass thus allowing it to dissolve <sup>21</sup>. An alteration layer can be  
155 observed on the surface of the glass in similar experiments under anoxic conditions, which is  
156 typically a gel layer and its thickness increases with time <sup>22,23</sup>. Most gel alteration layer (GAL)  
157 can be easily identified through the changes in the structure of the glass. During the  
158 dissolution of the glass, the process of hydrolysis is mostly responsible for the breaking of the  
159 Si-O-Si and Si-O-Zr bonds, therefore the number of bridging bonds decrease, while

160 hydroxides are formed. The end of the process is that the concentration of network formers  
161 decreases. As a result of hydration, the concentration of network modifiers components also  
162 changes <sup>24,21</sup>. The elemental composition of iron flakes did not change with time, corrosion  
163 products cannot be identified, and no sign of Fe-oxides formation was observed based on the  
164 SEM/EDX measurements. Spec8 (Fe edge position\*) in Table 4 shows that Fe and clay are  
165 simultaneously present at the measured position, no sign of Fe-oxide formation. Based on the  
166 literature data, iron corrosion products are usually present where a sufficiently large,  
167 continuous interface can be in contact with clay and glass interfaces. In such cases, in addition  
168 to Fe, there is also significant amount of oxygen, and a small amount of Si is also present.  
169 Similar observations are reported in Ref. <sup>25, 26</sup>.

170 For further investigations, SEM/EDX elemental maps were collected on the GFeC-7M sample  
171 from two regions, one of 150×50 μm<sup>2</sup> including all three types of materials (Fig. 5) and a  
172 smaller area focused on Fe-clay boundaries (Fig. 6). Elemental maps provide information on  
173 the spatial distribution of elements in the areas of interest and show the quality and quantity of  
174 elements. Based on the images, the edge and the bulk of the glass particle are uniform, based  
175 on the element map, the Fe distribution measured at the edge of the Fe particle is not uniform,  
176 but this can be explained by the uneven edges, which can be observed on the SEM  
177 backscattered image (Fig. 6). The elemental maps recorded on 5 kV show that distribution of  
178 the Si and O components occurred homogeneously in the clay and glass phase. Grains with  
179 surplus of O and Si are present the clay. The heterogeneous character of the clay can be  
180 observed most significantly based on the distribution of K, Na, Mg and Ca.

181 Further SEM investigation with the combination of Focused Ion Beam (FIB) sample  
182 preparation with higher lateral resolution were conducted on the GFeC-7M sample to  
183 elucidate the influence of the presence of Fe or clay on the alteration layer thickness of the  
184 glass particles. The SEM image and the corresponding line profile of the EDX signals are  
185 shown in Fig. 7. The glass-forming Si, O and Ba remained rather uniformly distributed in the  
186 glass particle, as the beam passes to the surface of the clay, Al can be identified from the  
187 albite in the claystone. The non-homogeneous nature of the clay can be observed by the  
188 changing distribution of Si and O. The sudden count drop can be explained by the formation  
189 of a deep crack, which is shown in Fig. 7**b**.

190 *Elemental analysis of the leaching solutions*

191 The ICP-OES and IC results for the glass/steel/clay leachates are shown in Table 6. The pH  
192 values indicate a slight increase with time: 8.12 (GFeC-3M), 8.25 (GFeC-7M) and 8.27  
193 (GFeC-12M). Higher concentrations of K, B and Na can be observed in the liquid phase of  
194 all three glass/steel/clay systems compared to the initial porewater. The temperature effect  
195 could not be ruled out when experiencing elevated concentrations since the conditioning of  
196 Boda claystone with the applied synthetic porewater was carried out at room temperature.  
197 However, as our experimental setup contains not only argillaceous rocks, leaching from the  
198 other components (Fe, glass) should also be considered. Elevated Si, B and Na concentrations  
199 from the baseline can be traced back to glass content, while the increased K content came  
200 from the claystone, which contains 4.7 wt%  $K_2O$ <sup>27</sup>. High Si content was measured at three  
201 months, after which the concentration decreased by an order of magnitude during the  
202 remaining course of the experiment. The concentration of Si and B developed similarly during  
203 the corrosion test, the concentration of both elements increased from the seventh to twelfth  
204 month. In contrast to this trend, in the case of Na, it can be observed that it increases until the  
205 seventh month, after which its concentration in the leachate decreases. Concentrations of  
206 bivalent cations including Ca and Mg decreased and the concentration of K increased one  
207 order of magnitude even after three months. A potential precipitation of potassium silicate  
208 species could be one explanation for the decreased concentration, but as a triplicate setup was  
209 applied, differences between individual containers can occur. Concentrations of  $Cl^-$  and  $SO_4^{2-}$   
210 ions in the final porewater are close to those of the conditioned SBPW but a slight increase  
211 was observed over time. The increase was less than 10% for  $Cl^-$  but more than 30% for  $SO_4^{2-}$ .

212 Table 7. indicates the normalized mass loss and glass dissolution rate for boron for the GFeC-  
213 7M and GFeC-12M samples. The obtained dissolution rates show a decreasing tendency in  
214 function of time in both sample series. B is usually assumed to provide the best measure of  
215 the extent of glass reaction as a consequence of its high solubility. The release of B occurred  
216 at an average rate of 0.0054 g/(m<sup>2</sup>d) until 7 months and 0.0011 g/(m<sup>2</sup>d) from 7 to 12 months.  
217 The boron concentration in the GFeC-12M leachate sample is 45.52 weight ppm which  
218 suggests that there was no significant change in the structure of the glass during the long  
219 experimental period (in the studied borosilicate glass, B has a role of network former). Our  
220 previous leaching results on this borosilicate glass also show an order of magnitude greater  
221 normal mass loss with similar  $SA/V$  ratio. In that series of experiments 0.079 g/(m<sup>2</sup>d)  
222 normalized mass loss was measured<sup>28</sup>. PCT-B test results on International Simple Glass (ISG)  
223 under acidic to hyperalkaline conditions were calculated mass loss after 120 days for B was

224 0.0131 g/(m<sup>2</sup>d), which is consistent to our previously achieved results <sup>29</sup>. Results of a similar  
225 order of magnitude are also true for the borosilicate glass K-26, on which 0.0405 g/(m<sup>2</sup>d)  
226 normalized leaching rate was measured <sup>30</sup>. These low values for our glassy samples can be  
227 explained by the fact that in the present experiments the borosilicate glass did not come into  
228 direct contact with the leaching fluid as in most product consistency test, only in indirect  
229 contact thanks to the fully saturated clay with SBPW. It can be predicted that the saturated  
230 iron and clay mixture present in the system does not promote the chemical degradation of the  
231 glasses, therefore our glassy structure is not damaged.

### 232 *X-ray Photoelectron Spectroscopy for glass surface characterization*

233 Composition of the prepared samples were investigated by measuring the surface in “as  
234 received“ state by XPS. It determines the composition of the upper ~5 nm. To observe the  
235 depth dependence of composition in the near surface region, ion sputtering combined XPS  
236 analysis was applied until stable concentration was reached. Because of the insulating nature  
237 of samples, a continuous double (+ and -) charge compensation was applied to prevent  
238 electrical charging up. The surface curvature of the glass samples resulted in an uneven  
239 charging that could be reduced by decreasing analyzed spot size to 200 μm, the measured spot  
240 was at the center of the sputtered square.

241 The 3 spots of G-2M showed a relatively larger variation of composition while the G-3M  
242 spots were essentially identical. The calculated composition (atomic %) is shown in Table 8  
243 (only the average value is shown where more measurements took place). Table 8 shows a  
244 value where the concentration was stable, or the change of concentration with depth where it  
245 was observed. The glass character of the samples has been remained even after the end of the  
246 treatment period. Sodium content was reduced significantly due to SBPW treatment which is  
247 consistent with our ICP-OES results, where it is also noted that after 3 months the initial  
248 conditioned SBPW's sodium content has increased significantly, from 492 mg/l to 610.7 mg/l  
249 as seen in Table 6. A significant part of this results from the very high albite content of the  
250 BCF mineral (43 wt%), but the contribution from the dissolution of the glass system cannot  
251 be neglected <sup>19</sup>. Ca is absent in G-Ref sample and its presence is uncertain on G-1M sample  
252 because of overlapping peaks, nonetheless 0.5-1% of Ca is possible. For demonstration, the  
253 Ca region of the XPS spectrum is shown in Fig. 8 for all 4 samples (G-Ref, G-1M, G-2M, G-  
254 3M). G-2M and G-3M samples have lower Mg content and higher Ca, and it allows the  
255 separation of Ca doublet undoubtedly. B content was not detected in any of the samples;  
256 however, the G-Ref sample has an intense Ba peak at B 1s energy, which prevents the

257 observation of a small B content. Another explanation for this phenomenon is that a possible  
258 evaporation process takes place on the surface of the melt, the rate of which depends on the  
259 partial water vapor pressure in the furnace atmosphere as discussed in Ref. <sup>31</sup>. Detection limit  
260 of B is ~0.2 at% in general, however, in case of G-Ref it is estimated 0.5 at%. Detected  
261 spectra of the 4 samples presenting the B region are shown in Fig. 8. Similar leaching  
262 experiments, where the value of  $SA/V$  was the same, large release was also measured in the  
263 initial stage for boron, since leaching can most easily occur from the regions close to the  
264 surface, therefore boron cannot be detected at this depth, as it is not present there <sup>32</sup>. Zr was  
265 observable in each sample, with a sudden Zr concentration drop in G-2M. The smearing of Zr  
266 3d peak is possibly due to some surface charging. Significant Mg appearance can be observed  
267 in G-1M sample. This phenomenon can be explained by Mg-silicate precipitation, which can  
268 be realized by the presence of magnesium in the leaching solution (Table 2). This phase is  
269 limited by the glass alteration kinetics and a pH above 8 is required for the phase formation <sup>20</sup>  
270 <sup>33</sup>. The pH of the leachates was 12.48, 9.64 and 8.91, for G-1M, G-2M and G-3M,  
271 respectively. In addition, after 2 months, precipitation is caused not only by Mg, but also by  
272 Ca, the concentration of which also increases in the case of G-2M and G-3M samples as  
273 shown in Table 8, similar results are presented in Ref. <sup>34</sup>. The detected C signal belongs to  
274 alkane compounds which exclude the presence of CO<sub>3</sub> as well.

275 SEM measurements were also carried out on the surface of the G-Ref, G-1M, G-2M and G-  
276 3M samples, and the results are shown in Fig. 9 **a-d**. The crystallized white agglomerates  
277 which are rich in Ca and Mg can be observed in Fig. 9 **b-d** starting from the G-1M sample  
278 and represent the precipitated magnesium and calcium silicate formation. Degradation of the  
279 glass surface can be observed as the experiment progresses, the most prominent change is  
280 shown on G-2M sample, which had cracks on its surface as a result of rapid cooling after the  
281 end of the experiment. Beside the cracks, the formation of a silica-rich gel layer can be  
282 observed on the sample's surface, started as small independent regions but at the end of the  
283 treatment this passivating layer is already continuous and homogeneous. As a result of the  
284 layer, the dissolution rate decreases as the mass transfer from the solid phase to the liquid  
285 phase will be limited <sup>35</sup>.

## 286 **Conclusion**

287 We investigated the effect of the materials/conditions of the modelled engineered barrier  
288 system on each other, using promising EBS materials under conditions predictable for their  
289 lifetime. During the SEM investigations – after 3, 7 and 12 months – the glass, Fe and clay

290 materials could be identified and investigated separately. Along the glass, the surface and  
291 borders do not vary. The main elements contained in borosilicate glass are Si, O, Na, Zr, Ba,  
292 and all of them with EDX analysis were detected after 3, 7 and 12 months. Although, no  
293 secondary phases were identified and no alteration layer has been found on the borosilicate  
294 glass samples in any case within the resolution of backscattered electron imaging at 20 keV  
295 ( $\sim\mu\text{m}$ ), the elemental composition of the investigated material changes in rather small  
296 amounts. That means the average composition within its information depth ( $\sim 1\ \mu\text{m}$ ) was not  
297 altered due to experimental treatment. Supplementary surface analysis was carried out with  
298 XPS directly on the 55mol%SiO<sub>2</sub>-10mol%B<sub>2</sub>O<sub>3</sub>-25mol%Na<sub>2</sub>O-5mol%BaO-5mol%ZrO<sub>2</sub>  
299 matrix glass to observe changes and possibly secondary phases formation. The results showed  
300 that the atomic composition remained rather the same in the case of Si and O after 3 months,  
301 while Na and Ba decreased. The presence of boron within the information depth cannot be  
302 detected. The most significant finding was the precipitation of Mg and Ca on the surface of  
303 the borosilicate glass resulting from the synthetic porewater. The formation of the passive  
304 layer can be observed, which takes on an increasingly homogeneous structure as time  
305 progresses. The ICP-OES results shows that the released fraction of B increases. The  
306 concentration of leached Ca and Mg among the glass-forming elements decreases which  
307 correlates with the XPS results, while the concentration of K, Si and Na increases. Ion  
308 chromatography measurement returned the initial concentration of the main ions, the  
309 concentration of Cl<sup>-</sup> and SO<sub>4</sub><sup>2-</sup> ions did not increase significantly even during the long  
310 experiment duration.

311 According to the results, we can conclude that under the tested conditions (12 Months, 80 °C)  
312 the used components of the engineered barrier system do not have a significant effect on each  
313 other, they individually preserve their integrity, which is the basic principle of Defense in  
314 Depth. The borosilicate glass remains a stable glass under the tested conditions, no sign of  
315 secondary phase formation and no measurable physical/chemical changes are observed. Fe  
316 flakes show no corrosion reaction. Based on our triplicate test, the minerals of BCF albitic  
317 claystone does not react with the other two engineered barriers and significantly slows down  
318 the structural transformation of the glass by delaying the alteration process.

## 319 **Methods**

320 *Scanning Electron Microscopy measurements*

321 During the Scanning Electron Microscopy with the combination of Energy Dispersive X-ray  
322 Spectroscopy (SEM/EDX) investigations, we mainly focused on the composition and the  
323 nature of alteration products formed on the Fe, within the clay and on the borosilicate glass  
324 surface. Measurements were performed using a Thermo Scientific Scios2 dual beam  
325 analytical FIB-SEM with an Oxford X-Max 20 SDD EDX attachment. The surface of the  
326 pellets was polished and covered with a thin carbon coating to improve the imaging of the  
327 samples and to avoid charge accumulation of the glass surface during electron beam  
328 investigations. Samples measured with an accelerating voltage of 20 kV and a beam current of  
329 1.6 nA. During the imaging of the GFeC-3M and GFeC-7M samples, the backscattered  
330 electrons were detected, therefore the heavier elements appear brighter since these elements  
331 backscatter more strongly, in the case of GFeC-12M sample, the secondary electrons were  
332 detected.

333 Focused Ion Beam (FIB) instrument was used as a sample preparation tool to mill into the  
334 surface of the material to provide cross-sectional analysis of the GFeC-7M sample. The cross-  
335 section of the surface layers was investigated to observe the penetration depth of the  
336 porewater and to reveal any changes in the elemental composition. Before milling, a 2-3  $\mu\text{m}$   
337 thick Pt protective layer was applied to the surface using 2 kV electrons then 30 kV Ga-ions.  
338 Then a trench was milled perpendicular to the surface using the FIB beam. The imaging of the  
339 trench was performed with SEM by tilting the sample to 45° from the normal vector of the  
340 surface, all results were corrected by the effect of the tilting. The line profile of EDX signals  
341 was measured at 20 kV.

#### 342 *Leaching test*

343 Normalized release and glass dissolution rate were calculated for boron with the following  
344 equations based on ASTM C1285-21 protocol to gain information on the chemical evolution  
345 of the studied system and determine the chemical durability of the homogeneous glass waste  
346 form by measuring the concentration of the elements released to the synthetic porewater <sup>36</sup>:

$$NL_B = \frac{c_B(\text{sample})}{(f_B) \cdot \left(\frac{SA}{V}\right)} \quad (1)$$

$$NR_B = \frac{c_B(\text{sample})}{(f_B) \cdot \left(\frac{SA}{V}\right) \cdot (t)} \quad (2)$$

347 where  $c_B$  is the concentration of boron in the given soaking water (g/l),  $f_B$  is the weight fraction  
348 of the boron in the original borosilicate glass (unitless),  $\frac{SA}{V}$  is the surface area of the final  
349 waste form divided by the volume of the leachate ( $m^{-1}$ ) and  $t$  is the duration of the  
350 experiment (days).

### 351 *Inductively Coupled Plasma Optical Emission Spectroscopy and Ion Chromatography*

352 Inductively Coupled Plasma Optical Emission Spectroscopy (ICP-OES) and Ion  
353 Chromatography (IC) investigations were performed on the aqueous solutions. 5 ml of the  
354 leachates were sampled from the liquid phase located in the outer Teflon container after 3, 7  
355 and 12 months. The collected leachates are filtered through 0.45  $\mu m$  cellulose acetate  
356 membrane. B, Ca, K, Mg, Na and Si were measured using a Perkin Elmer Avio 200 ICP-OES  
357 apparatus, all the elements were measured in radial view and Y was used as the internal  
358 standard. Ion chromatography was applied for  $Cl^-$  and  $SO_4^-$  concentration determination. For  
359 ion chromatography a Thermo Scientific Dionex Aquion instrument was used with an A23  
360 ( $2 \times 250 \text{ mm}^2$ ) column and a guard column (AS23  $2 \times 250 \text{ mm}^2$ ) for  $Cl^-$  and  $SO_4^-$  concentration  
361 determination. The applied eluent was 4.5 mM  $Na_2CO_3$ / 0.8 mM  $NaHCO_3$  with  
362 electrochemical suppressing (AERS 500 Carbonate). The injection volume was 1 ml and the  
363 initial samples were diluted to 1000 times for the IC analysis.

### 364 *X-ray Photoelectron Spectroscopy*

365 X-ray Photoelectron Spectroscopy is a proper technique for measuring elemental composition  
366 in the surface region. As the photoelectrons are emitted from the sample under X-ray  
367 irradiation, the elements and their valance state can be measured with high reliability within  
368 its information depth  $\sim 3 \text{ nm}$  and with lower sensitivity within  $\sim 10 \text{ nm}$ .

369 The used system was an Escalab Xi<sup>+</sup> equipment of Thermo Fisher Scientific Inc.. The basic  
370 vacuum level ( $1 \times 10^{-10}$  mbar) was weakened to  $2 \times 10^{-7}$  mbar during ion sputtering  
371 measurements. The ion sputtering was achieved with a 500 eV  $Ar^+$  beam with 45° angle of  
372 incidence scanned over  $2 \text{ mm} \times 2 \text{ mm}$  area. These sputtering conditions provided about 2 nm  
373 removal in 1 step. Beside of the main component lines, namely Si 2p (92eV) and O 1s (532  
374 eV) several assumed minor components were observed with lines such as B 1s (186eV), Ca  
375 2p (350eV), Ba 3d (780eV), Zr 3d (182eV) as well as 3p (336eV), S 2p (164eV), K 2p  
376 (292eV), Mg KL2 (310eV), Na 1s (1072eV), C 1s (284 eV).

377 Measurements started on G-Ref and G-1M samples using 900  $\mu m$  X-ray spot and was altered  
378 to 200  $\mu m$  spot because of unsatisfactory charge compensation at this spot size. G-2M and G-

379 3M samples were measured with 200  $\mu\text{m}$  spot size. To improve the reliability of the measured  
380 composition, more location on the surface was observed as follows: 1 position for G-Ref, 4  
381 position with 900  $\mu\text{m}$  and 1 position repeated with 200  $\mu\text{m}$  for G-1M, 3 position with 200  $\mu\text{m}$   
382 for G-2M and 3 position with 200  $\mu\text{m}$  for G-3M. Measured spectra were evaluated by  
383 determining the peak intensities. Decomposition of complex peak shapes with peak fitting  
384 algorithm were applied where necessary:

385 - B: B 1s interferes with Zr 3d doublet and Ba 4p 1/2.

386 - Ca 2p: interferes with Zr 3p 1/2 and Mg KL4 (Auger).

387 Component concentration was calculated with sensitivity factors from ALTHERMO1 library  
388 by assuming homogeneous target. The XPS spectra included a carbon signal that weakened  
389 with reaching larger depth. Since the carbon signal belonged to hydrocarbon state without  
390  $\text{CO}_3$ , we assumed the carbon is a surface contamination and not a material component. Thus,  
391 carbon was excluded from the evaluation.

### 392 **Acknowledgements**

393 The research was supported by the European Joint Programme on Radioactive Waste  
394 Management (EURAD) Assessment of chemical evolution of ILW and HLW disposal cell  
395 (ACED) work package (EU grant agreement number: 847593). One of the authors (M.F.)  
396 acknowledge that this project was partly supported by the János Bolyai Research Scholarship  
397 of the Hungarian Academy of Sciences. The authors are grateful to N. Szasz who performed  
398 the SEM/EDX measurements.

### 399 **Author contributions**

400 I.T. performed the ICP-OES measurements and leaching tests and calculations and prepared  
401 the manuscript; O.J. evaluated the SEM/EDX measurements and edited the final manuscript;  
402 O.Cz. prepared the samples and performed the IC analysis; A.S. performed the XPS  
403 measurements; M.F. conceptualization, methodology, prepared the samples, and edited the  
404 final manuscript, funding acquisition.

### 405 **Competing interests**

406 The authors declare no competing interest.

### 407 **Data availability statement**

408 All data generated or analyzed during this study are included in this published article.

409 **References**

- 410 Information Library - World Nuclear Association. [available on 30.01.2023,  
411 <https://www.world-nuclear.org/information-library/country-profiles.aspx>.]
- 412 Hill, S. L. W. The Corrosion of Carbon Steel under Deep Geologic Nuclear Waste Disposal  
413 Conditions. *Electronic Thesis and Dissertation Repository*. 3820.  
414 <https://ir.lib.uwo.ca/etd/3820> (2016).
- 415 Valković, V. The nuclear fuel cycle. in *Radioactivity in the Environment* 329–396 ISBN: 978-  
416 0-444-64146-5 (Elsevier, 2019). doi:10.1016/b978-0-444-64146-5.00006-9
- 417 IAEA Safety Standards Storage of Spent Nuclear Fuel for protecting people and the  
418 environment No. SSG-15 Specific Safety Guide. [available on 30.01.2023, [http://www-](http://www-ns.iaea.org/standards/)  
419 [ns.iaea.org/standards/](http://www-ns.iaea.org/standards/)].
- 420 Baratova, D., Neča, V. Multi-Barrier System Model of the Geological Repository for Spent  
421 Nuclear Fuel. *Nuclear-2016* 6–12 (2016).
- 422 Bennett, D. Engineered Barrier Systems and the Safety of Deep Geological Repositories  
423 *European Commission Organisation For Economic Co-Operation And Development*. ISBN  
424 92-64-18498-8 (2003).
- 425 Mohapatra, M. & Manchanda, V. K. Characterization of borosilicate glass as host matrix for  
426 high level waste. *IOP Conf Ser Mater Sci Eng* **2**, 012006 (2009).  
427 doi:10.1088/1757-899X/2/1/012006
- 428 Jantzen, C. M. Development of glass matrices for high level radioactive wastes. Handbook of  
429 Advanced Radioactive Waste Conditioning Technologies (Woodhead Publishing Limited,  
430 2011). doi:10.1533/9780857090959.2.230
- 431 Raj, K. & Kaushik, C. P. Glass matrices for vitrification of radioactive waste - An update on  
432 R & D efforts. in *IOP Conference Series: Materials Science and Engineering* **2**, 012002  
433 (2009). doi:10.1088/1757-899X/2/1/012002
- 434 Crusset, D. *et al.* Corrosion of carbon steel components in the French high-level waste  
435 programme: evolution of disposal concept and selection of materials. *Corrosion Engineering*  
436 *Science and Technology* **52**, 17–24 (2017). doi:10.1080/1478422X.2017.1344416

- 437 Thorpe, C. L. *et al.* Forty years of durability assessment of nuclear waste glass by standard  
438 methods. *Materials Degradation* **5** (2021). doi:10.1038/s41529-021-00210-4
- 439 Asmussen, RM. *et al.* *Evaluation of Degradation Mechanisms for Solid Secondary Waste*  
440 *Grout Waste Forms*. [available on 30.01.2023, <https://www.ntis.gov/about>] (2021).
- 441 Fabian, M., Svab, E., Proffen, T. & Veress, E. Structure study of multi-component  
442 borosilicate glasses from high-Q neutron diffraction measurement and RMC modeling. *J Non*  
443 *Cryst Solids* **354**, 3299–3307 (2008). doi:10.1016/j.jnoncrysol.2008.01.024
- 444 Nemeth, T. *et al.* Clay mineralogy of the Boda Claystone Formation (Mecsek Mts., SW  
445 Hungary). *Open Geosciences* **8**, 259–274 (2016). doi:10.1515/geo-2016-0024
- 446 Somodi, G., Krupa, A., Kovacs, L. Comprehensive rock mechanical characterization of BAF-  
447 1, -1A, 1Af and BAF-2 boreholes *Bodai Agyagko Formacio kutatas* 61-66 (2018). [in  
448 Hungarian] A BAF-1, -1A, 1Af furasi szelveny es a BAF-2 furas kozetmechanikai szempontu  
449 ertekelese
- 450 Lazar, K. & Mathe, Z. Claystone as a Potential Host Rock for Nuclear Waste Storage. *Clay*  
451 *Minerals in Nature - Their Characterization, Modification and Application* (2012).  
452 doi:10.5772/48123
- 453 Bradbury, M. H. & Baeyens, B. *Contaminant Hydrology A mechanistic description of Ni and*  
454 *Zn sorption on Na-montmorillonite Part II: modelling. Baeyens / Journal of Contaminant*  
455 *Hydrology* **27** (1997).
- 456 Bradbury, M. H., Baeyens, B., Pearson, F. & Berner Addendum, U. *TECHNICAL REPORT*  
457 *97-07 Derivation of In Situ Opalinus Clay Porewater Compositions from Experimental and*  
458 *Geochemical Modelling Studies* (1997).
- 459 Varga, A., Raucsik, B., Szakmany, G. & Mathe, Z. Mineralogical, petrological and  
460 geochemical characteristics of the siliciclastic rock types of Boda Siltstone Formation.  
461 *Foldtani Kozlony* **136**, 1–31 (2006). [in Hungarian] A Bodai Aleurolit Formacio tormelekes  
462 kozettipusainak asvanytani, kozettani es geokemiai jellemzoi
- 463 Frugier, P. *et al.* SON68 nuclear glass dissolution kinetics: Current state of knowledge and  
464 basis of the new GRAAL model. *Journal of Nuclear Materials* **380**, 8–21 (2008).  
465 doi:10.1016/j.jnucmat.2008.06.044

466 Manaktala, H. K. An Assessment of Borosilicate Glass as a High Level Waste Form. *Center*  
467 *for Nuclear Waste Regulatory Analyses San Antonio, Texas* NRC-02-88-005 (1992).

488 Necib, S., Linard, Y. Martin E. Burger, P. Jollivet, S. Dewonck, C. Iron/clay/glass interaction  
469 in compacted clay at 50°C. 2–3 (2015). doi:10.13140/RG.2.1.2060.1206

470 de Combarieu, G. *et al.* Glass-iron-clay interactions in a radioactive waste geological  
471 disposal: An integrated laboratory-scale experiment. *Applied Geochemistry* **26**, 65–79 (2011).  
472 doi:10.1016/j.apgeochem.2010.11.004

473 Carriere, C. *et al.* Influence of iron corrosion on nuclear glass alteration processes: nanoscale  
474 investigations of the iron-bearing phases. *Corrosion Engineering Science and Technology* **52**,  
475 166–172 (2017). doi: 10.1080/1478422X.2017.1306962

476 Carriere, C. *et al.* The fate of Si and Fe while nuclear glass alters with steel and clay. *Npj*  
477 *Mater Degrad* **5**, 16 (2021). doi:10.1038/s41529-021-00160-x

478 Carriere, C. *et al.* Use of nanoprobes to identify iron-silicates in a glass/iron/argillite system in  
479 deep geological disposal. *Corros Sci* **158**, 108104 (2019). doi:10.1016/j.corsci.2019.108104

480 Toth, E., Hrabovszki, E., Toth, T. M. & Schubert, F. Shear strain and volume change  
481 associated with sigmoidal vein arrays in the Boda Claystone. *J Struct Geol* **138**, 104105  
482 (2020). doi:10.1016/j.jsg.2020.104105

483 Fabian, M., Pinakidou, F., Tolnai, I., Czompoly, O. & Osan, J. Lanthanide (Ce, Nd, Eu)  
484 environments and leaching behavior in borosilicate glasses. *Sci Rep* **11**, 1–15 (2021).  
485 doi:10.1038/s41598-021-92777-w

486 Backhouse, D. J. *et al.* Corrosion of the International Simple Glass under acidic to  
487 hyperalkaline conditions. *Npj Mater Degrad* **2**, 1–10 (2018). doi:10.1038/s41529-018-0050-5

488 Ojovan, N. V. *et al.* Product consistency test of fully radioactive high-sodium content  
489 borosilicate glass K-26. *Materials Research Society Symposium Proceedings* **824**, 339–344  
490 (2004). doi:10.1557/PROC-824-CC8.14

491 van Limpt, *et al.* Modelling the evaporation of boron species. Part 1. Alkali-free borosilicate  
492 glass melts. *Glass Technology - European Journal of Glass Science and Technology Part A*.  
493 **52**. 77-87 (2011).

494 Ledieu, A., Devreux, F., Barboux, P., Sicard, L. & Spalla, O. Leaching of borosilicate glasses.  
495 I. Experiments. *J Non Cryst Solids* **343**, 3–12 (2004). doi:10.1016/j.jnoncrsol.2004.06.006

496 al Dabbas, A. & Kopecko, K. Corrosion of ISG by Mg-Si precipitation in presence of  
497 Ankerite. *Pollack Periodica* **17**, 56–61 (2022). doi:10.1556/606.2021.00410

498 Chinnam, R. K., Fossati, P. C. M. & Lee, W. E. Degradation of partially immersed glass: A  
499 new perspective. *Journal of Nuclear Materials* **503**, 56–65 (2018).  
500 doi:10.1016/j.jnucmat.2018.02.040

501 Gin, S. *et al.* A General Mechanism For Gel Layer Formation On Borosilicate Glass Under  
502 Aqueous Corrosion. *J. Phys. Chem. C* **124**, 9, 5132-5144 (2020).  
503 doi:10.1021/acs.jpcc.9b10491

504 ASTM C1285-21 Standard Test Methods for Determining Chemical Durability of Nuclear ,  
505 Hazardous , and Mixed Waste Glasses and Multiphase Glass Ceramics : The Product  
506 Consistency Test ( PCT ) **1**. 1–22 (2005). doi:10.1520/C1285-21

507

508

509 **Figure legends**

510 Fig. 1 Cross-section view of the experimental setup indicating the different materials. Filled  
511 inner containers with the glass/steel/clay mixture and the external containers with the  
512 assembled inner container.

513 Fig. 2 **a, b** SEM backscattered electron images on the GFeC-3M sample after 3 months.  
514 Several spectra of glass particles (a) and Fe flakes (b) were measured (solids of interest are  
515 marked as gl: glass, cl: clay and Fe).

516 Fig. 3 **a, b** SEM backscattered electron images on GFeC-7M sample after 7 months (solids of  
517 interest are marked as gl: glass, cl: clay and Fe). Several spectra of each materials (a) and  
518 spectras mainly focusing on Fe-clay boundaries (b).

519 Fig. 4 Secondary electron image of a characteristic area on GFeC-12M sample after the end of  
520 the treatment.

521 Fig. 5 **a, b** SEM backscattered electron image (a) and the corresponding EDX elemental maps  
522 on the GFeC-7M sample (b).

523 Fig. 6 **a, b** Backscattered electron image (a) from a smaller area zoomed on Fe-clay  
524 boundaries and the corresponding elemental maps on the GFeC-7M sample (b)

525 Fig. 7 **a, b, c** SEM image of a focused ion-beam cross-section of the glass parts (a), SEM  
526 image (b) and the line profile of the EDS signals of the GFeC-7M sample (c) measured at  
527 20kV.

528 Fig. 8 **a, b** The Ca-Zr-Mg region (a) and for the B-Ba region (b) of the XPS spectrum can be  
529 observed for all samples: G-Ref (blue), G-1M (yellow), G-2M (green) and G-3M (red).

530 Fig. 9 **a, b, c, d** Backscattered electron images at 800× magnification on the surface of G-Ref  
531 (a), G-1M (b), G-2M (c) and G-3M (d) samples

532 **Tables**

533 **Table 1.** Mineralogical composition of the albitic claystone section of the BAF-2 drilling core  
 534 of BCF.

<b>Mineral composition</b>	<b>[wt%]</b>
Vermiculite	2
Illite	24
Chlorite	6
Quartz	7
Albite	43
K-feldspar	<LOD
Calcite	5
Dolomite	8
Hematite	6

535

536 **Table 2.** Chemical composition of synthetic Boda porewater (SBPW).

<b>Element, ion</b>	<b>Concentration (mol/L)</b>
Na	$1.7 \times 10^{-2}$
K	$1.8 \times 10^{-4}$
Mg	$2.3 \times 10^{-3}$
Ca	$3.1 \times 10^{-3}$
Sr	$1.5 \times 10^{-5}$
Cl <sup>-</sup>	$2.3 \times 10^{-2}$
SO <sub>4</sub> <sup>2-</sup>	$1.9 \times 10^{-3}$
HCO <sub>3</sub> /CO <sub>3</sub>	$6.1 \times 10^{-4}$
<b>Other parameters</b>	
Ionic strength (mol/L)	$3.3 \times 10^{-2}$
pH	8.1
Eh (mV)	-300

537

538 **Table 3.** SEM/EDX results: elemental composition at selected positions after 3 months (wt.  
 539 %).

<b>Elements</b>	<b>Spec1 (gl)</b>	<b>Spec2 (grain in</b>	<b>Spec3 (gl)</b>	<b>Spec4 (Fe)</b>	<b>Spec5 (gl)</b>
-----------------	-----------------------	----------------------------	-----------------------	-----------------------	-----------------------

claystone)					
<b>O</b>	43.89	50.18	44.82		43.27
<b>Na</b>	4.84	5.69	4.53		3.87
<b>Mg</b>		0.42			
<b>Al</b>		11.70	0.37		
<b>Si</b>	26.79	28.45	25.01		29.38
<b>K</b>		2.48	0.30		
<b>Fe</b>				100	0.67
<b>Zr</b>	8.15		9.23		7.57
<b>Ba</b>	16.33		15.73		15.24
<b>Total</b>	100	100	100	100	100

540

541 **Table 4.** SEM/EDX results: elemental composition at selected positions after 7 months (wt.  
542 %).

<b>Elements</b>	<b>Spec1</b> (Fe)	<b>Spec2</b> (gl)	<b>Spec3</b> (gl)	<b>Spec4</b> (grain in claystone)	<b>Spec7</b> (Fe edge position)	<b>Spec8</b> (Fe edge position*)	<b>Spec9</b> (Fe edge position)
<b>O</b>	0.44	38.02	43.63	44.66	1.26	29.12	5.82
<b>Na</b>		4.65	5.07	2.24			
<b>Mg</b>				1.96			
<b>Al</b>	0.02	0.03		9.21		3.74	0.40
<b>Si</b>	0.13	23.04	31.59	27.85	0.21	8.30	0.85
<b>P</b>				0.15			
<b>K</b>		2.48		4.21		0.69	
<b>Ca</b>						0.85	
<b>Fe</b>	99.39			6.59	98.53	57.30	92.93
<b>Zr</b>		9.35	7.17				
<b>Ba</b>		20.39	12.04				
<b>N</b>	0.02	0.14					
<b>B</b>		4.37					
<b>Total</b>	100	100	100	100	100	100	100

543

544 **Table 5.** SEM/EDX results: elemental composition at selected positions after 12 months (wt.  
545 %).

<b>Elements</b>	<b>Spec1</b> (Fe)	<b>Spec2</b> (gl)	<b>Spec3</b> (gl)	<b>Spec4</b> (gl)	<b>Spec5</b> (gl)	<b>Spec6</b> (Fe-cl)	<b>Spec7</b> (Fe-cl)	<b>Spec8</b> (Fe)
<b>O</b>	1.01	47.23	43.79	42.81	45.82	47.96	10.79	
<b>Na</b>		5.87	4.21	3.55	3.39	2.57	0.82	

<b>Mg</b>		0.21		0.25	2.41	1.01		
<b>Al</b>		0.72	0.74	1.10	7.90	3.26		
<b>Si</b>	26.04	27.25	28.06	26.81	21.49	6.48		
<b>K</b>		0.33	0.50	0.45	2.19	1.23		
<b>Ca</b>		0.26	0.55	0.26	0.72	1.33		
<b>Fe</b>	98.99	0.64	0.58	0.53	14.15	75.07	100.00	
<b>Zr</b>	8.41	8.90	10.12	8.38				
<b>Ba</b>	12.44	13.70	13.08	13.01	0.60			
Total	100	100	100	100	100	100	100	100

546

547 **Table 6.** ICP-OES and IC results of GFeC-3M, GFeC-7M and GFeC-12M liquid phase  
548 samples.

	<b>B</b>	<b>Ca</b>	<b>K</b>	<b>Mg</b>	<b>Na</b>	<b>Si</b>	<b>Cl<sup>-</sup></b>	<b>SO<sub>4</sub><sup>2-</sup></b>
	[mg/l]							
SBPW recipe	-	125	7	57	380	-	81 7	182
SBPW conditioned	0.12	108	22	49	492	5.9	82 3	183
GFeC-3M	n.a.	59.4	232.2	28	610.7	101.8	83 0	234
GFeC-7M	39.72	64.71	163.45	27.01	713.6	29.83	84 1	246
GFeC-12M	45.52	64.48	162.58	23.83	673.01	40.79	89 1	280

549

550 **Table 7.** Normalized mass loss and glass dissolution rate for boron.

	<b>C(B)</b>	<b>f(B)</b>	<b>SA/V</b>	<b>NC(B)</b>	<b>NL(B)</b>	<b>d<sub>eq</sub>(B)</b>	<b>r</b>
	[g/l]	-	[m <sup>-1</sup> ]	[g/l]	[g/m <sup>2</sup> ]	[μm]	[g/(m <sup>2</sup> d)]
GFeC-7M	39.72	0.032	1101.4	1.251	1.14	0.43	0.0054
GFeC-12M	45.52	0.032	1101.4	1.434	1.31	0.49	0.0011

551

552 **Table 8.** The calculated composition (atomic%) from the results of XPS measurements

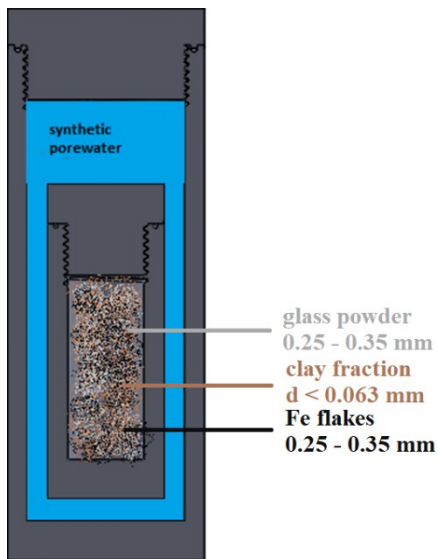
	<b>G-Ref</b>	<b>G-1M</b>	<b>G-2M</b>	<b>G-3M</b>
Si	27.1	24.5	22.8	24.9
O	63.1	65.4	64.3	65.2
Na	7.2=>4.8	1.1=>0.4	0.4	0.6=>0.13
Ca	~0	~0	2.1	2.2
Ba	1.0=>1.2	0.15	2.3	0.09
Zr	1.4=>1.6	2.1	0.4	4.0
K	2.1	0.2	~0	0.4
Mg	~0.1	7.2	5.8	2.9
B	~0	~0	~0	~0

---

S	$\sim 0$	$\sim 0$	2.7	$\sim 0$
---	----------	----------	-----	----------

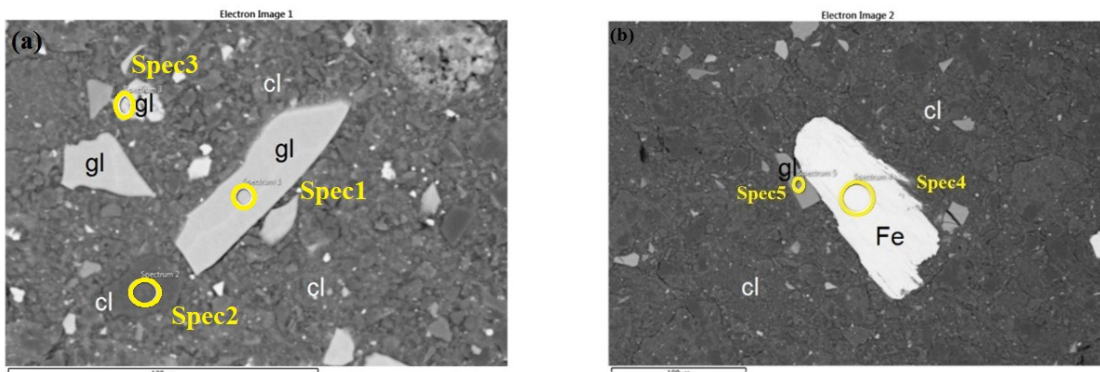
---

554 **Figures**



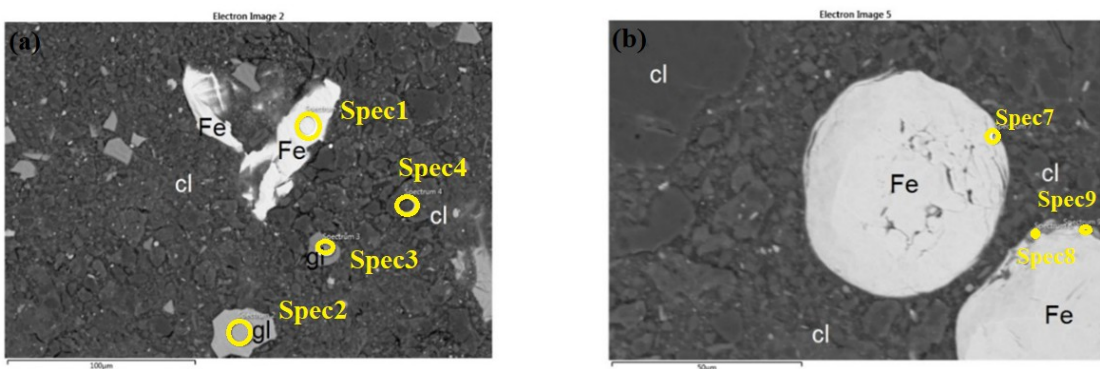
555 **Fig. 1** Cross-section view of the experimental setup

556



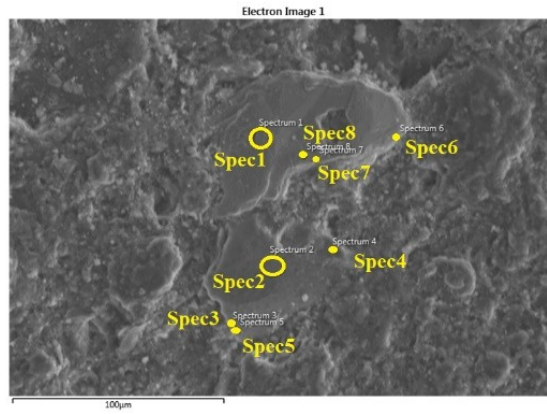
557 **Fig. 2 a. b** SEM backscattered electron images on the GFeC-3M sample.

558



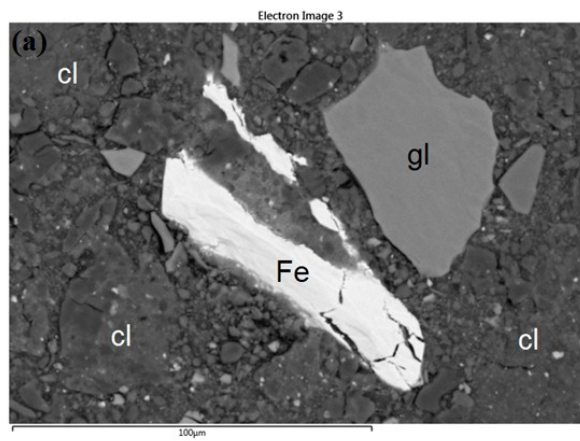
559 **Fig. 3 a. b** SEM backscattered electron images on GFeC-7M sample.

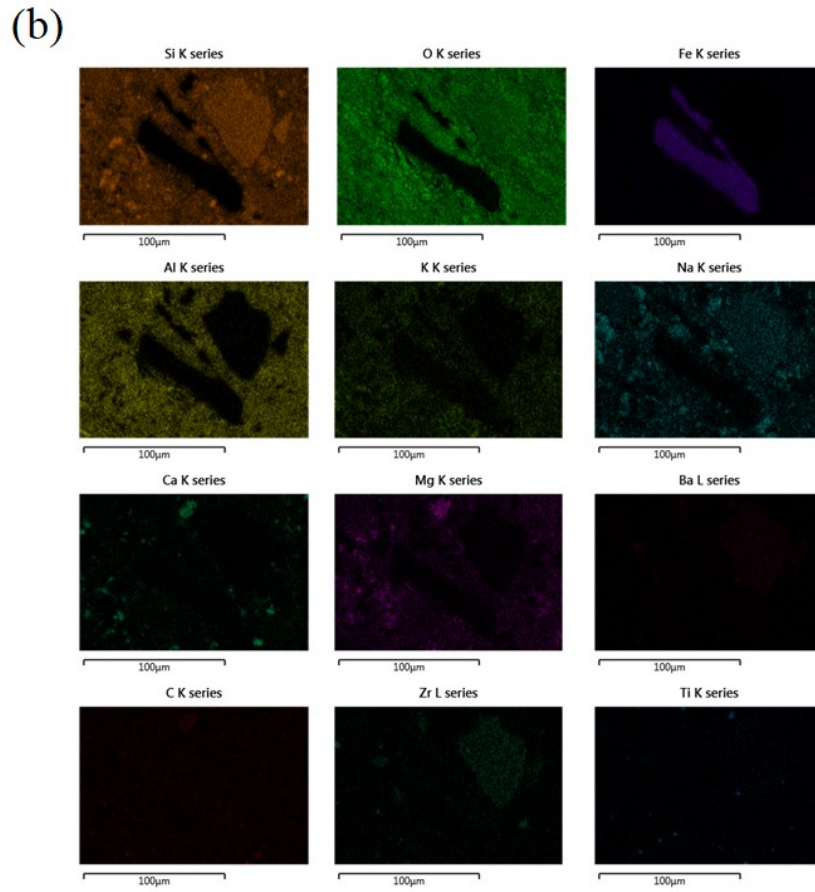
560



561 **Fig. 4** SEM secondary electron image on GFeC-12M sample.

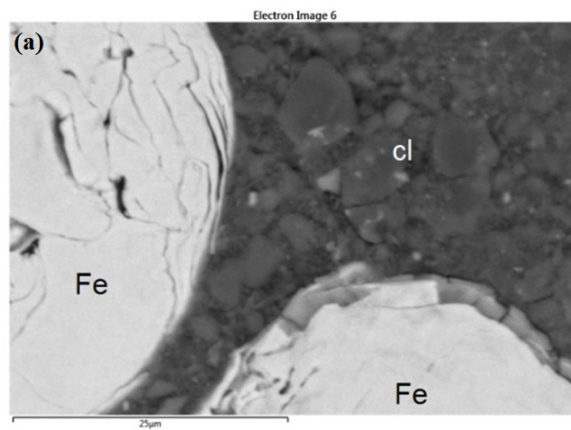
562

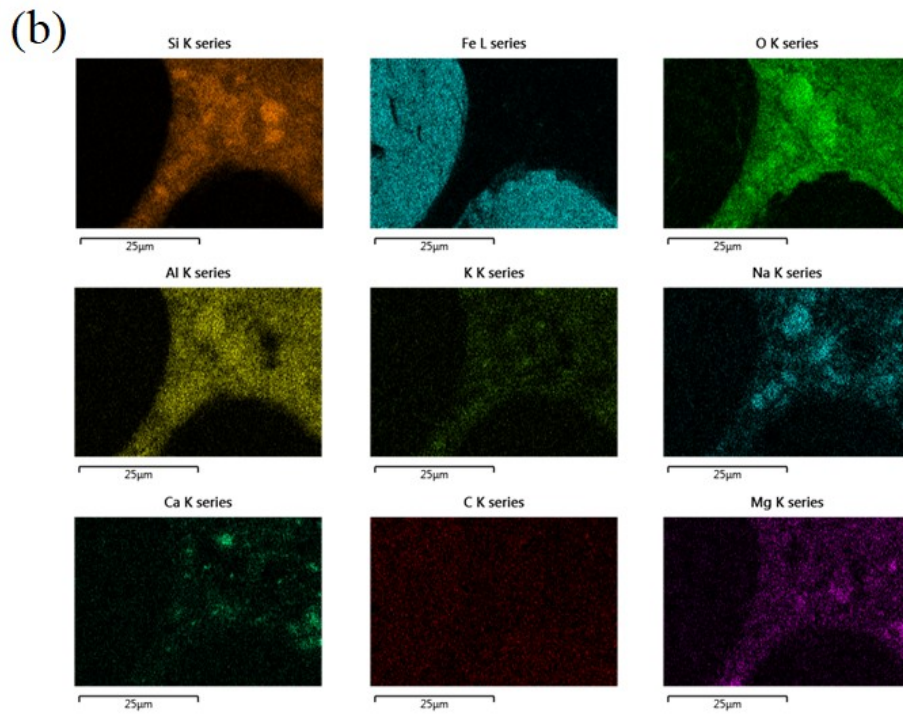




563 **Fig. 5 a. b** SEM backscattered electron image and the corresponding EDX elemental maps on  
 564 the GFeC-7M sample.

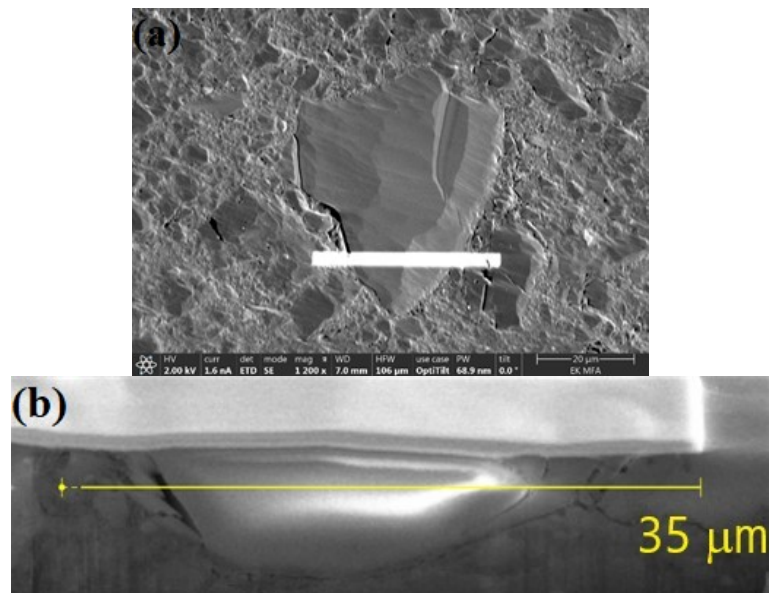
565

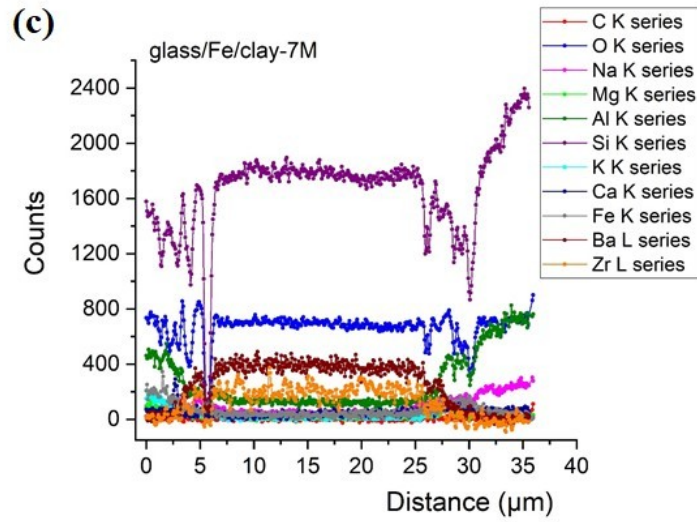




566 **Fig. 6 a. b** SEM backscattered electron image and EDX elemental maps from Fe-clay  
 567 boundaries on sample GFeC-7M.

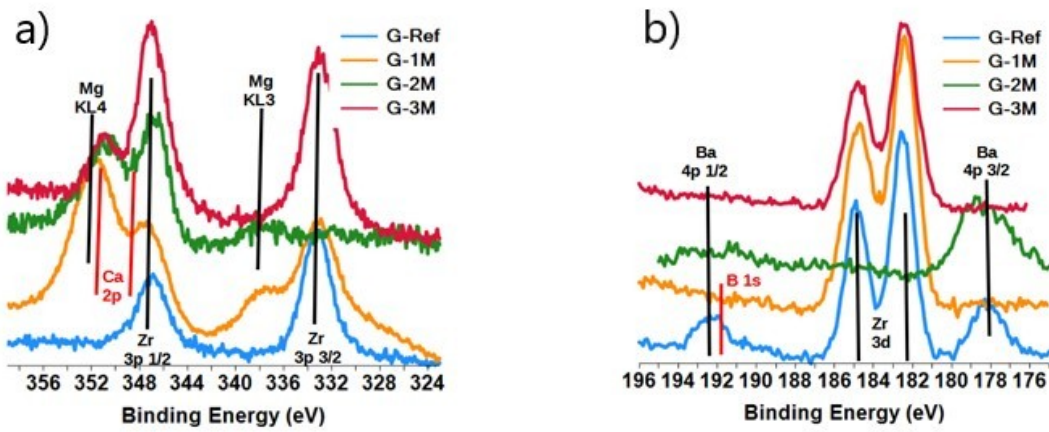
568





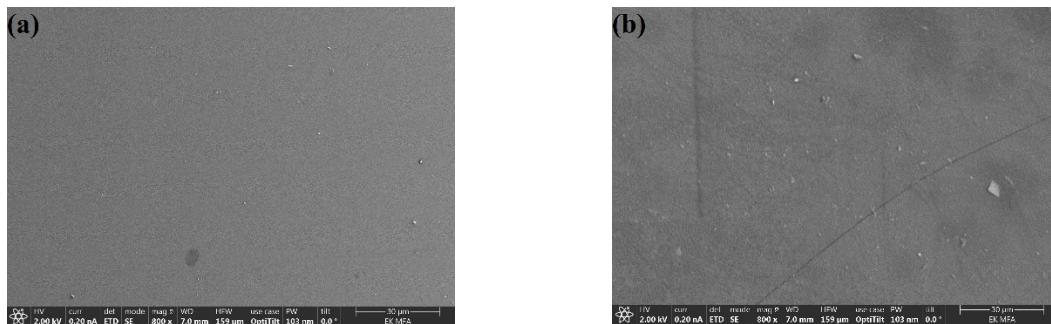
569 **Fig. 7 a. b. c** SEM image and line profile of the GFeC-7M sample.

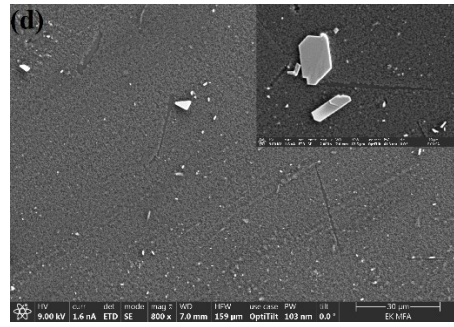
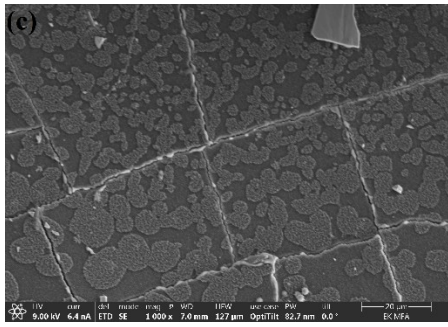
570



571 **Fig. 8 a. b** Ca-Zr-Mg region (a) and B-Ba region (b) of the XPS spectrum for G-Ref, G-1M,  
572 G-2M and G-3M samples

573





574 **Fig. 9 a. b. c. d** SEM secondary electron images on the glassy G-Ref (a), G-1M (b), G-2M (c)  
575 and G-3M (d) samples.